Ocean Modelling 32 (2010) 132–142

Contents lists available at ScienceDirect

Ocean Modelling

journal homepage: www.elsevier.com/locate/ocemod

A "vortex in cell" model for quasi-geostrophic, shallow water dynamics on the sphere

A. Mohammadian *, John Marshall

Department of Earth, Atmospheric and Planetary Science, Massachusetts Institute of Technology, Cambridge, MA, USA

ARTICLE INFO

Article history:
Received 15 July 2009
Received in revised form 29 December 2009
Accepted 4 January 2010
Available online 1 February 2010

Keywords:
Geostrophic turbulence
Reduced gravity
Lagrangian
Vortex in cell
Quasi-geostrophic

ABSTRACT

The vortex in cell (VIC) method has been found to be an attractive computational choice for solving a number of fluid dynamical problems. The Lagrangian advection of particles leads to stability of the method even for long time steps. Moreover, conservation of particle properties, such as potential vorticity, can be enshrined at the heart of the numerical procedure. In this paper we describe a numerical implementation of the VIC method for a reduced gravity, quasi-geostrophic model and make use of its novel aspects to explore the interaction of waves and turbulence on the sphere. The Lagrangian advection of particles is performed using a fourth order Runge–Kutta method and the stream-function is obtained by the inversion of potential vorticity using an underlying Eulerian grid. The scheme is tested in the simulation of Rossby and Rossby–Haurwitz waves. Encouraging results are obtained for various radii of deformations corresponding to both the atmosphere and ocean.

1. Introduction

Here we experiment with algorithms for numerical solution of a quasi-geostrophic system in which the fluid is represented by a large number of discrete particles whose potential vorticities are treated as the primary variable. Various numerical approaches are available for solution of vorticity-stream function equations, to which the quasi-geostrophic system belongs. These include finite difference, finite volume, finite element, Lagrangian/semi-Lagrangian, spectral and vortex methods. Among these, spectral and vortex methods are most commonly used for turbulence studies where a low level of numerical damping and oscillatory behavior is crucial. In direct numerical simulations (DNS) Cottet et al. (2002) showed that the 'vortex in cell' (VIC) method exhibits good results at large and intermediate scales, whilst avoiding accumulation of energy at the end of spectrum in under-resolved cases. Spectral methods are not well suited to the study of domains in the presence of boundaries where Legendre-type polynomials are usually used which are very expensive. Vortex methods, on the other hand, have proved useful in study of a wide range of turbulent flows and domains: computational cost is only slightly increased in the presence of boundaries (Cottet and Koumoutsakos, 2000; Cottet et al., 2002). Despite offering a natural way of modeling oceanic and atmospheric flows, however, vortex methods have been rarely used in our field. Hence our interest in exploring them here.

Many variants of vortex methods have been employed in the wider computational literature. Their common feature is that the vorticity is represented by "elements" (e.g. point vortices or using a chosen basis function), which are tracked in the domain using Lagrangian methods, an elegant and robust way to treat the nonlinear advection terms. The main idea in vortex methods is to compute the trajectories of the particles, advect the point vortices, and compute the flow field based on the new position of the vortices. Inspired by the method of computing the flow field from point vortices, two main groups of vortex methods may be identified. In the first, sometimes called the 'grid-free' vortex method, the flow field is directly obtained from the point vortices using the Biot–Savat law (see, for example Lakkis and Ghoniem, 2009; Huang et al., 2009). This approach becomes computationally prohibitive as the number of particles becomes very large, since the velocity field acting on each point vortex is induced by all other point vortices. However, fast methods may reduce the cost of this step to $O(N\log N)$ or $O(N)$, where N is the number of elements. In the second approach, known as the 'vortex in cell' (VIC) method and originally developed by Christiansen (1973), the flow field is obtained by solving a Poisson equation using an underlying Eulerian grid (as sketched in Fig. 1).

The VIC method has been widely used in the simulation of complex fluid dynamical problems. Liu and Doorly (1999) used it successfully for cavity flows driven by impulsively-started and oscillating lids, including vortex/wall interactions. Ould-Salihi et al. (2000) showed that the VIC method, with appropriate

* Corresponding author.
E-mail addresses: majidm@mit.edu, majid.mohammadian@uottawa.ca (A. Mohammadian).

1463-5003/$ - see front matter © 2010 Elsevier Ltd. All rights reserved.
doi:10.1016/j.ocemod.2010.01.001

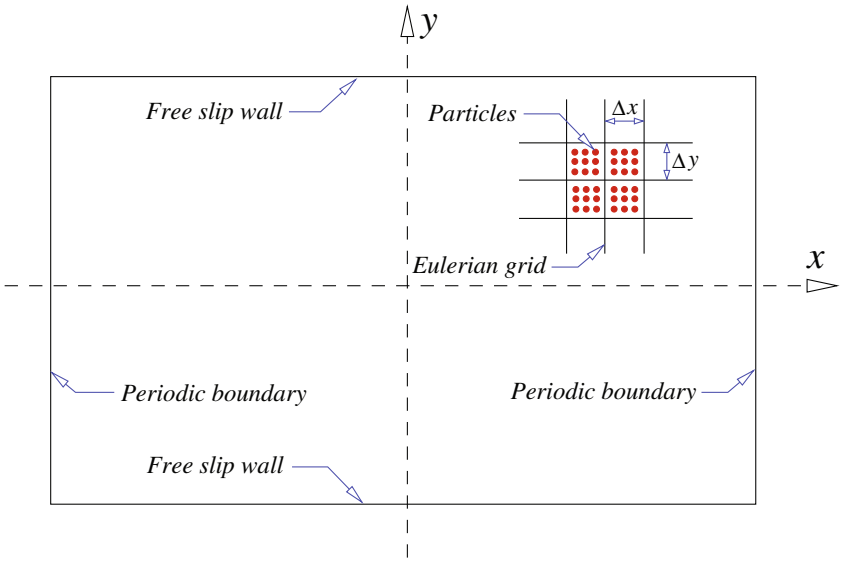

Fig. 1. The 'vortex in cell' method follows the trajectories, and computes the potential vorticity of discrete particles as they move over an underlying Eulerian grid. To compute particle trajectories, the vorticity on particles is interpolated to the Eulerian grid. This gridded vorticity is then inverted for the stream-function, from which the velocity is computed and interpolated back to the particle positions. This interpolated velocity is then used to compute new particle positions.

interpolation schemes and exploiting domain decomposition, are more effective than pure finite difference approaches for turbulent flows. Liu (2001) employed VIC for three-dimensional modeling of boundary layers under the impact of a vortex ring. Kudela and Regucki (2002) used VIC for simulation of leapfrogging phenomenon for two rings with the same circulation. Cottet and Poncet (2003) used the VIC method for simulation of wall-bounded turbulent flows with a body-fitted grid. Uchiyama and Naruse (2004) employed VIC to model free turbulent two-phase flows and concluded that it was computationally less expensive than the grid-free vortex method. Cocle et al. (2008) combined VIC and parallel fast multipole methods for efficient domain decomposition simulations of instability of vortex rings and space-developing wakes at very high resolution. Further applications of VIC can be found in the references of the above-mentioned studies.

The objective of this study is to explore VIC as a method of solution of a reduced gravity, quasi-geostrophic model on the sphere and evaluate its performance in simulating fundamental geophysical phenomena such as Rossby waves and turbulence in the atmosphere and ocean. A main feature of the model is that, in the absence of dissipation, the potential vorticity of particles is conserved (by construction) as in the continuous system. Moreover, the Lagrangian transport of the particles eliminates difficulties in the representation of advection such as nonlinear instabilities and time step restrictions associated with Eulerian methods. Other aspects of the VIC method includes the possibility of direct control on generation and dissipation of vortices (for example in the representation of baroclinic instabilities by eddies, see Sections 5 and 6) straightforward modeling of a mean background flow as explained below, and availability of trajectories at no extra cost (useful for estimation of eddy diffusivity). As illustrated herein, the VIC method can be successfully employed in the modeling of QG systems resulting in an efficient and accurate tool particularly in oceanographic applications where boundaries play a central role.

This paper is organized as follows. In Section 2 the quasi-geostrophic equations that will be solved are presented. Section 3 presents the VIC method and describes computational details for particle tracking and interpolation. In Section 4, Rossby and Rossby–Haurwitz test cases are studied and the results compared with analytical solutions. In Section 5 we apply the model to the study of the interaction of geostrophic turbulence and Rossby waves on the sphere. Some concluding remarks complete the study.

2. Continuous equations for a QG shallow water layer

The quasi-geostrophic equations representing the evolution of a shallow-water layer may be written in vorticity-stream function form as

$$Q = f + \nabla^2\psi - \frac{\psi}{L_d^2} \tag{1}$$

$$\frac{DQ}{Dt} = -\alpha\zeta \tag{2}$$

where $\zeta = \nabla^2\psi$ is relative vorticity, Q is potential vorticity, f is the Coriolis parameter, ψ is the stream-function, α is a dissipation coefficient and L_d is the radius of deformation. The term ψ/L_d^2 in Eq. (1) is a representation of vortex stretching. Eq. (2) states that in the absence of dissipation, potential vorticity remains constant following a particle. As we shall see, this property is at the core of the vortex in cell method.

The material derivative in (2) is defined as

$$\frac{D}{Dt} = \frac{\partial}{\partial t} + u^x\frac{\partial}{\partial x} + u^y\frac{\partial}{\partial y} \tag{3}$$

where u^x and u^y are, respectively, the zonal (eastward) and meridional (northward) velocity components of the flow in the rotating coordinate system. The velocity field $\mathbf{u} = (u^x, u^y)$ can be expressed in terms of particle positions and the stream-function thus:

$$(u^x, u^y) = \left(\frac{Dx}{Dt}, \frac{Dy}{Dt}\right) = \left(-\frac{\partial\psi}{\partial y}, \frac{\partial\psi}{\partial x}\right) \tag{4}$$

Eqs. (1), (2) along with (4) constitute the heart of our model. That is, given the initial potential vorticity of particles, the stream-function is obtained by solving the elliptic equation (1), particle trajectories are computed using (4) to displace particles to their new position, and the particle potential vorticities are updated using Eq. (2).

In spherical coordinates, changes in latitude $(d\theta)$ and longitude $(d\lambda)$ are given by

$$d\theta = \frac{dy}{R} \tag{5}$$

$$d\lambda = \frac{dx}{R\cos(\theta)} \tag{6}$$

where R is the radius of the sphere and dx, dy are changes in distance along latitude and longitude circles, respectively. Hence the angular velocity components (in rad/s) in λ and θ directions, respectively, are given by

$$u^{\lambda} = \frac{D\lambda}{Dt} = \frac{u^x}{R\cos(\theta)} = \frac{-1}{R}\frac{\partial\psi}{\partial\theta} \tag{7}$$

$$u^{\theta} = \frac{D\theta}{Dt} = \frac{u^y}{R} = \frac{1}{R\cos(\theta)}\frac{\partial\psi}{\partial\lambda} \tag{8}$$

In spherical coordinates, the elliptic equation relating ζ and ψ takes the following form:

$$\zeta = \nabla^2\psi = \frac{1}{R^2\cos^2(\theta)}\frac{\partial^2\psi}{\partial\lambda^2} + \frac{1}{R^2\cos(\theta)}\frac{\partial}{\partial\theta}\left(\cos(\theta)\frac{\partial\psi}{\partial\theta}\right) \tag{9}$$

Note that the numerical algorithm in spherical coordinates is exactly the same as in Cartesian coordinates except for geometric factors in the calculation of trajectories and inversion of the vorticity field. This greatly simplifies the numerical algorithm for integration of the above system. Our algorithm is described in the next section.

3. Numerical procedure using VIC

As represented schematically in Fig. 1, the VIC method lays down an Eulerian grid, seeds it with particles endowed with potential vorticity (pv) and advects those particles around. The pv on the particles is interpolated to the grid, where it is inverted for the currents. The currents are then interpolated back from the grid to the particles allowing their position to be stepped forward in time. The details of the algorithm we have devised and implemented is now described in detail.

3.1. Algorithm

The algorithm used for numerical integration from $t = 0$ to $t = n\Delta t$, where Δt is the time-step size, is summarized here. A schematic layout of the model is shown in Fig. 1. In the following, the notation $\mathbf{x}^n = RK4(\mathbf{x}^{n-1}, \mathbf{u}^n, \Delta t)$ indicates that $\mathbf{x}^n$ is the new position of the particles, initially at $\mathbf{x}^{n-1}$, computed using the flow field $\mathbf{u}^n$ over a time interval Δt by a RK4 method.

1. Initialize model with m particles in each cell and initialize their relative vorticity ζ_p^0 . The subscript p refers to particles. In the results presented here we set $m = 9$.
2. Given the initial position $\mathbf{x}^0$ and initial relative vorticity of particles ζ_p^0, for n = 1–N do:
   - 2-1. Interpolate relative vorticity of particles ζ_p^{n-1} to grid points ζ_c^{n-1} (the subscript c refers to grid points).
   - 2-2. Invert relative vorticity, $\psi^* = \nabla^{-2}\zeta_c^{n-1}$.
   - 2-3. Compute the flow field, $\mathbf{u}^* = \nabla^{\perp}\psi^*$.
   - 2-4. Using the fourth order RK method, advect the particles from the position $\mathbf{x}^{n-1}$ in the flow field $\mathbf{u}^*$ for a half time interval $\Delta t^* = \frac{\Delta t}{2}$, to obtain the intermediate position of particles $\mathbf{x}^*$, where $\mathbf{x}^* = RK4(\mathbf{x}^{n-1}, \mathbf{u}^*, \Delta t^*)$.
   - 2-5. Compute the intermediate potential vorticity Q^* using
     $$Q^* = Q^{n-1} - \Delta t^*\alpha\zeta^{n-1} \tag{10}$$
   - 2-6. Compute the relative vorticity ζ^* of the particles at the new position $\zeta^* = Q^* - f - \frac{\psi^*}{L_d^2}$, where f and ψ^* are, respectively, the Coriolis parameter and stream function at the intermediate position of particles $\mathbf{x}^*$.
   - 2-7. Interpolate intermediate relative vorticity of particles ζ_p^* to grid points ζ_c^*.
   - 2-8. Invert relative vorticity $\psi^{**} = \nabla^{-2}\zeta_c^*$.
   - 2-9. Compute the flow field $\mathbf{u}^{**} = \nabla^{\perp}\psi^{**}$.
   - 2-10. Using the fourth order RK method, advect the particles from the position $\mathbf{x}^{n-1}$ in the flow field $\mathbf{u}^{**}$ for a full time interval Δt , to obtain the new position of particles $\mathbf{x}^n$, where $\mathbf{x}^n = RK4(\mathbf{x}^{n-1}, \mathbf{u}^{**}, \Delta t)$.
   - 2-11. Compute the potential vorticity Q^n as $Q^n = Q^{n-1} - \Delta t\alpha\zeta^*$.
   - 2-12. Compute the relative vorticity ζ^n of the particles at the new position $\zeta^n = Q^n - f - \frac{\psi^n}{L_d^2}$, where f and ψ^n are, respectively, the Coriolis parameter and stream function at the new position of particles $\mathbf{x}^n$.

It should be mentioned that since we use a latitude–longitude grid, our gird converges at high latitudes. However, time-step size can remain large because the advection is performed using a Lagrangian method. Indeed, our main constraint in choosing time-step size is accuracy. Therefore, in order to benefit from the stability of the scheme for large time-step sizes, we use a fourth order scheme to calculate trajectories. Splitting methods can also be used. However, note that RK4 is efficient because we do not invert the vorticity field at each stage of RK4. Moreover, interpolation of the velocity field is not computationally expensive because a first order method is sufficient (see below).

3.2. Interpolation method

Interpolation is needed at various stages of the numerical method to transfer information from the Eulerian grid to particles and vice versa. The following methods are employed.

3.2.1. Interpolation of velocity field from the Eulerian grid to particles

As explained above, a first order accurate scheme (Christiansen, 1973) was employed to interpolate the velocity field from the Eulerian grid to particles. Consider the particle k at the position

$$(x_p^k, y_p^k) = \big((i+\delta_x)\Delta x, (j+\delta_y)\Delta y\big) \tag{11}$$

where Δx and Δy are the Eulerian grid sizes in x and y directions, respectively. The velocity at the point (x_p^k, y_p^k) is computed as

$$\mathbf{u}(x_p^k, y_p^k) = A_1^k\mathbf{u}(i,j) + A_2^k\mathbf{u}(i+1,j) + A_3^k\mathbf{u}(i,j+1) + A_4^k\mathbf{u}(i+1,j+1) \tag{12}$$

where

$$A_1^k = (1-\delta_x)(1-\delta_y), \qquad A_2^k = \delta_x(1-\delta_y) \tag{13}$$

$$A_3^k = (1-\delta_x)\,\delta_y, \qquad A_4^k = \delta_x\,\delta_y \tag{14}$$

3.2.2. Interpolation of ζ or $Q - f$ from particles to the Eulerian grid

Since the Coriolis parameter f can be exactly computed at the position of particles, we do not interpolate the potential vorticity Q from particles to the Eulerian grid. Instead we may interpolate either $Q - f$ or relative vorticity ζ. The interpolation of ζ is computationally more expensive because the quantity $\frac{\psi}{L_d^2}$ is known on the Eulerian grid and must be interpolated first to the position of particles to compute the relative vorticity of point vortices. However, as shown in the following, for the oceanic regimes where ζ is typically much smaller than $\frac{\psi}{L_d^2}$, interpolation of $Q - f$ leads to considerable error in the vorticity field. It is thus necessary to interpolate ζ rather than $Q - f$.

Interpolation from particles to the Eulerian grid is typically done using the so-called area method (Appendix A). However, we

found that this can lead to inaccuracies in the phase speed of Rossby waves. Instead we use an 'inverse distance' method to interpolate from particles to the Eulerian grid, as follows. The main idea is that the vorticity of each particle in our method is an approximation of the vorticity of the fluid at that point and by advection of particles we are indeed using a Lagrangian method. The particles in our method are not Dirac Delta point vortices as in grid-free vortex methods. The spatial distribution of vorticity of the fluid can therefore be approximated using any averaging method based on the known vorticity at the position of particles. We chose to use the 'inverse distance' interpolation method because the gain in accuracy from using higher order methods was justified compared to simply increasing the resolution of the grid.

We consider an Eulerian grid point at the position $(i\Delta x, j\Delta y)$. Let N be the number of particles for which (see Fig. 1)

$$(i-1)\Delta x < x_p^k < (i+1)\Delta x, \quad k = 1, \ldots, N \tag{15}$$

$$(j-1)\Delta j < y_p^k < (j+1)\Delta y, \quad k = 1, \ldots, N \tag{16}$$

Then, ζ_{ij}, the relative vorticity at the Eulerian grid point (i,j), is computed as

$$\zeta_{ij} = \frac{\sum_{k=1}^{N} \zeta^k / s^k}{\sum_{k=1}^{N} 1/s^k} \tag{17}$$

where s^k is the distance of the particle k from the Eulerian grid point (i,j)

$$s^k = \sqrt{\left(x_p^k - i\Delta x\right)^2 + \left(y_p^k - j\Delta y\right)^2} \tag{18}$$

3.2.3. Interpolation of the stream function from the Eulerian grid to particles

The velocity field on the Eulerian grid is obtained by a second order central difference scheme as

$$u^{\lambda}(i,j) = -\frac{\psi(i,j+1) - \psi(i,j-1)}{2R^2 \cos(\theta_j)\Delta\theta} \tag{19}$$

$$u^{\theta}(i,j) = \frac{\psi(i+1,j) - \psi(i-1,j)}{2R^2 \cos(\theta_j)\Delta\lambda} \tag{20}$$

A free slip boundary condition is employed at northern and southern boundaries.

The velocity on the Eulerian grid is then interpolated to the particles as described in Section 3.2.1. The accuracy of interpolating $\frac{\psi}{L_d^2}$ from the Eulerian grid to particles is found to be crucial for oceanic parameters and thus a high order accurate interpolation scheme is needed. Here, an efficient interpolation is employed in which the two-dimensional interpolation is preformed using a sequence of one-dimensional cubic interpolations. Precisely, first $\psi((i+\delta_x)\Delta x, k\Delta y)$, $k = j-1, \ldots, j+2$ is computed using a cubic Lagrange interpolation of $\psi(i-1,k)$, $\psi(i,k)$, $\psi(i+1,k)$ and $\psi(i+2,k)$ in the zonal direction (see Appendix A). Finally, a meridional cubic interpolation is performed on $\psi((i+\delta_x)\Delta x, k\Delta y)$, $k = j-1, \ldots, j+2$ to compute $\psi((i+\delta_x)\Delta x, (j+\delta_y)\Delta y)$.

3.3. Inversion of elliptic operator on Eulerian grid

A centered second order five-point finite difference scheme is used to discretize the elliptic equation (1) as

$$\zeta(i,j) = \frac{\psi(i+1,j) - 2\psi(i,j) + \psi(i-1,j)}{R^2 \cos^2(\theta_j)\Delta\lambda^2} + \frac{\cos(\theta_{j+1/2})(\psi(i,j+1) - \psi(i,j)) - \cos(\theta_{j-1/2})(\psi(i,j) - \psi(i,j-1))}{R^2 \cos(\theta_j)\Delta\theta^2} \tag{21}$$

The resulting system may be solved using a variety of available direct or iterative methods. Here, a preconditioned conjugate gradient algorithm is used to solve the linear system (using ADI preconditioning). For oceanic cases where L_d is small, the term ψ/L_d^2 is dominant and thus the algorithm converges within a few iterations.

3.4. Boundary conditions

Free slip boundary conditions are assumed for the northern and southern boundaries of the spherical domain, i.e. the meridional velocity is set to zero at those boundaries. Thus, particles are not allowed to leave the domain through the southern and northern boundaries. The periodic boundary conditions in the zonal direction is implemented as follows. Each particle that leaves the left or right boundary, reenters the domain from the other side. In order to simplify the interpolation procedure, ghost cells are considered at the left and right boundaries and particles are copied in the ghost cells from the corresponding cells in the other side. This greatly simplifies the computations since a unique interpolation procedure is employed for all Eulerian grid points.

4. Tests of the numerical method

In this section, several numerical experiments are presented to evaluate the performance of the algorithm described in the previous section. We simulate the propagation of Rossby waves on a β-plane and on a sphere in barotropic ($L_d = \infty$) and baroclinic (finite L_d) cases. We also describe how to prescribe mean flows and study their influence on the evolution of the point vortices. Both a β-plane channel and spherical coordinate are implemented. The spherical model uses a latitude–longitude grid, where latitude ranges from -80° to 80° and latitude from 0° to 360°.

4.1. Rossby waves on the β-plane

We first consider barotropic Rossby waves on a β-plane in a periodic domain of size $L \times L$, and thus set $\psi/L_d = 0$. The equation of potential vorticity (2) in this case is reduced to

$$\frac{\partial \zeta}{\partial t} + J(\psi, \zeta) = -\beta v \tag{22}$$

A solution of (22) is the Rossby wave given by

$$\psi = a \sin(kx - \omega t) \sin ly \tag{23}$$

with the frequency

$$\omega = \frac{-\beta k}{k^2 + l^2} \tag{24}$$

The vorticity in this case takes the following form

$$\zeta = -(k^2 + l^2)\psi \tag{25}$$

and so $\mathbf{u} \cdot \nabla\zeta = 0$. Thus, Eq. (23) is a solution of the full nonlinear system. Here, we initialize the system using (23) with $k = l = 4\pi/L$ and amplitude $a = 5.1 \times 10^5$ m^2/s. An Eulerian mesh with 400 grid point in each direction is employed. The initial condition and the numerical result (presented as a Hovmöller diagram) is shown in Fig. 2. As can be seen the model can readily simulate the movement of the Rossby wave with an accurate phase speed. Comparisons of analytical and numerical solutions for the Rossby wave at $t = 2\pi/\omega$ with 100×100 , 200×200 grid and 400×400 grids are shown in Fig. 3. As can be seen, the numerical error in phase speed at the coarse grid (100×100) becomes vanishingly small as the grid is refined.

It should be mentioned that we have experimented with the number of particles required to seed the cells and found that at least one particle should be in each cell at all times. Should a cell become devoid of particles, new ones can be introduced at the center of that cell. The vorticity of the new particles is obtained using a cubic

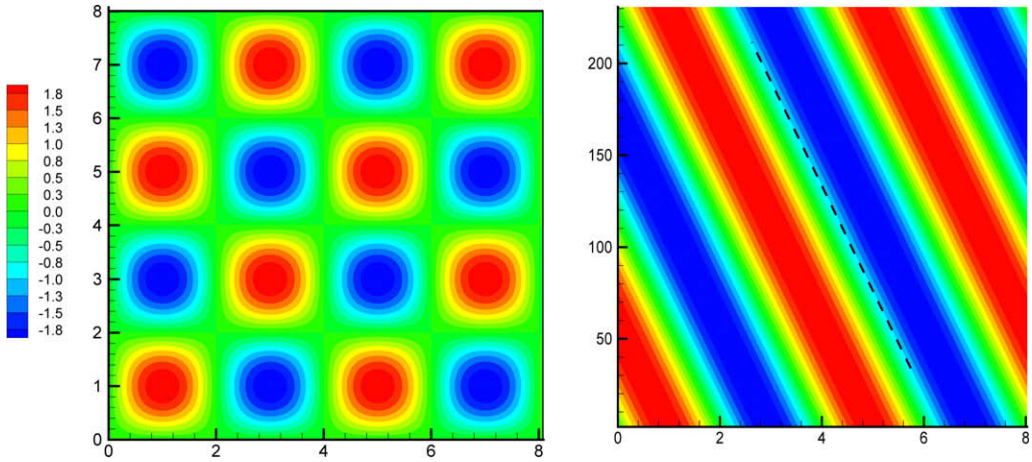

Fig. 2. Left: Initial Rossby waves at $t = 0$. Colors show stream-function in 10^5 m^2/s. Horizontal and vertical axes represent distance in 10^6 m . Right: Hovmöller diagram at $y = 5 \times 10^6$ m. Horizontal axis is distance in 10^6 m and vertical axes is time in days. The bold dashed line represents analytical slope.

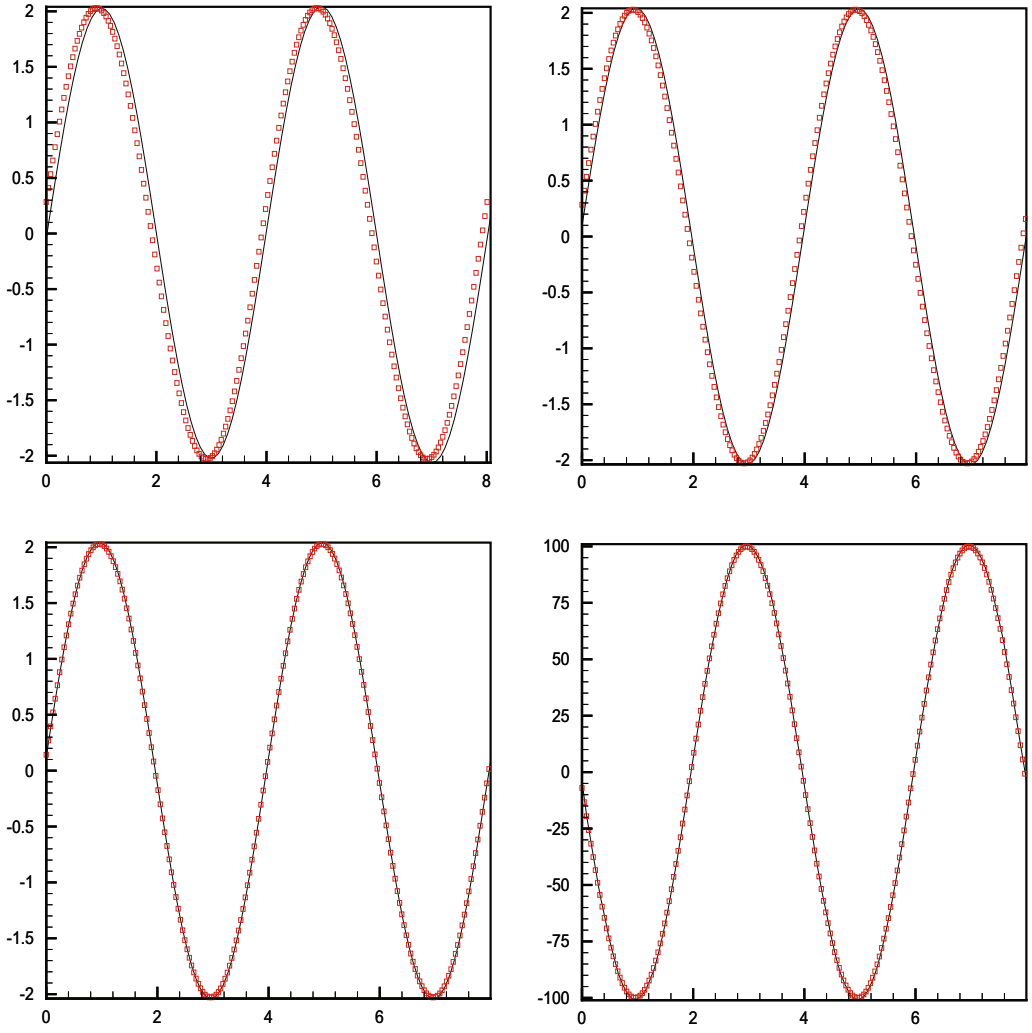

Fig. 3. Comparison of analytical and numerical solutions for the Rossby wave at $t = 2\pi/\omega$. Horizontal axes represent distance in 10^6 m. Squares show the numerical result and continuous curves show analytical solution. Top left: Stream-function in 10^5 m^2/s with a 100×100 grid; top right: stream-function in 10^5 m^2/s with a 200×200 grid; bottom left: stream-function in 10^5 m^2/s with a 400×400 grid; bottom right: relative vorticity (in 10^{-8} s^{-1}) with the 400×400 grid.

interpolation from the Eulerian grid. Note that this is consistent with our interpretation of particles and our interpolation method used to calculate vorticity at the Eulerian grid from particles. In the calculations shown here, we began with nine particles in each cell.

4.2. Rossby waves on the sphere

The second numerical experiment deals with Rossby waves on the sphere. The Coriolis parameter in this case is given by

$$f = 2\Omega \cos\theta \tag{26}$$

where $\Omega = 2\pi\ \text{day}^{-1}$ is the angular velocity of Earth's rotation. The Rossby wave solution now has the following form

$$\psi = -a \sin\theta \cos^m\theta \cos(m\lambda - \omega t) \tag{27}$$

with a frequency given by

$$\omega = \frac{-2m\Omega}{(1+m)(2+m)} \tag{28}$$

Again we note that $\mathbf{u}\cdot\nabla\zeta = 0$ and so the above solution also satisfies the nonlinear equations. First, we set $\psi/L_d = 0$ and choose Rossby wave number $m = 4$, as suggested by Williamson et al. (1992). An Eulerian mesh with, respectively, 304 and 128 grid points in the zonal and meridional directions is employed. Numerical results are shown in Fig. 4a demonstrating that the model can successfully simulate the propagation of Rossby waves on the sphere.

4.2.1. Effects of a finite deformation radius

4.2.1.1. Atmosphere. We now repeat the last test but this time turn on the ψ/L_d term to represent the effect of vortex stretching. We leave it to the reader to verify that the Rossby–Haurwitz solution is still valid but now with a phase speed given by

$$\omega = \frac{-2m\Omega + bmR^2\Omega}{(1+m)(2+m)} \tag{29}$$

with

$$b = \frac{2}{L_d^2(1+m)(2+m) + R^2} \tag{30}$$

That is, the Rossby–Haurwitz wave is slowed down in the presence of a finite deformation radius. This furnishes us with a good nonlinear test solution (since $J(\psi,\zeta) = 0$) for validation of our numerical technique when the radius of deformation L_d is not zero. We choose $L_d = 1000$ km as a typical atmospheric case and set $a = 4.1\times10^7$ m^2/s. Numerical results at time $t = 2\pi/\omega$ are presented in Fig. 4b. No visible noise or damping is observed which confirms the accuracy of the model for atmospheric parameters.

4.2.1.2. Ocean. In the previous test cases, the quantity $\zeta - \psi/L_d^2$ was interpolated from particles to the Eulerian grid using a linear scheme and yielded satisfactory results. In the oceanic case, however, we find that such a simple approach is not sufficiently accurate. We consider a typical oceanic case with $L_d = 100$ km and $a = 10^6$ m^2/s. Note the phase speed in this cases is ~100 times slower than the atmospheric test. Thus, numerical modeling of the oceanic case is much more demanding since small numerical errors can accumulate during such slow dynamics. Results using linear interpolation of $\zeta - \psi/L_d^2$ are shown in Fig. 4.c and reveals unacceptable numerical noise. This is because the relative vorticity ζ is now much smaller than ψ/L_d^2 and errors in the interpolation of ψ/L_d^2 lead to spurious values of ζ. To overcome this problem, we choose to interpolate the relative vorticity from particles to the Eulerian grid and then add in the vortex stretching term after interpolation.

This leads to a considerable improvement even with a linear interpolation (not shown). We found that a cubic interpolation of ψ/L_d^2 from the Eulerian grid to particles worked well—see Fig. 4d. Note that due to the structured form of the Eulerian grid, a high order accurate interpolation from the Eulerian grid to particles is less expensive than the high order accurate interpolation from particles to the Eulerian grid. Comparisons of analytical and numerical solutions for the Rossby–Haurwitz wave with cubic interpolation of ζ for the case $L_d = 100$ km at $t = 2\pi/\omega$ are presented in Fig. 5 which shows that the model can well simulate the wave. Finally, note that noise in the vorticity field is filtered in the inversion of potential vorticity and smooth results are obtained for stream function and potential vorticity (not shown).

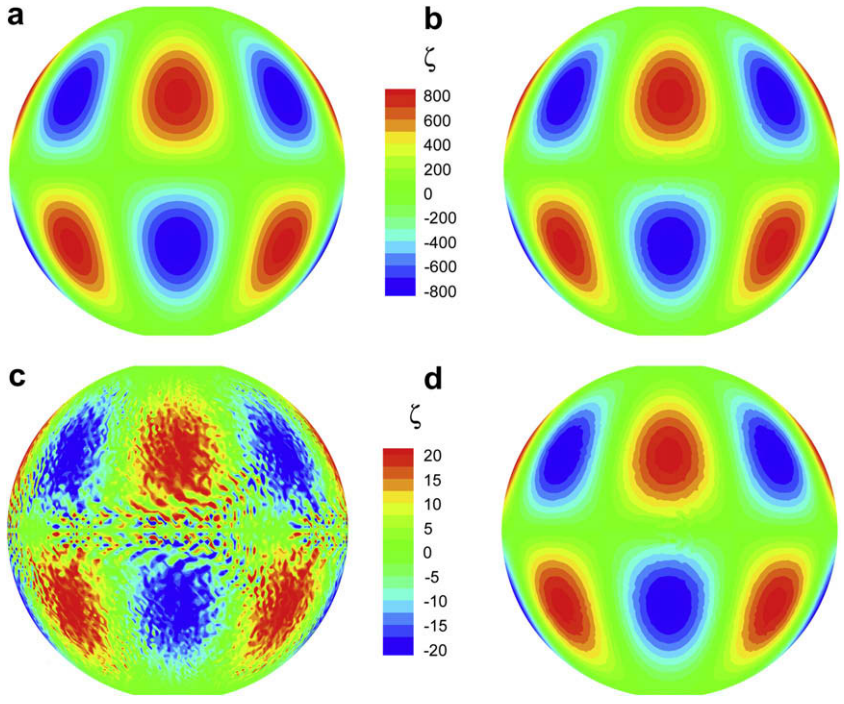

Fig. 4. (a) Relative vorticity (in 10^{-8} s^{-1}) for the case $\psi/L_d = 0$ at $t = 2\pi/\omega$ (i.e. after one Rossby wave cycle). (b) Relative vorticity (in 10^{-8} s^{-1}) for the case $L_d = 1000$ km at $t = 2\pi/\omega$. (c) Relative vorticity (in 10^{-8} s^{-1}) with linear interpolation of $\zeta - \psi/L_d^2$ for the case $L_d = 100$ km at $t = 2\pi/\omega$. (d) Relative vorticity (in 10^{-8} s^{-1}) with cubic interpolation of ζ for the case $L_d = 100$ km at $t = 2\pi/\omega$.

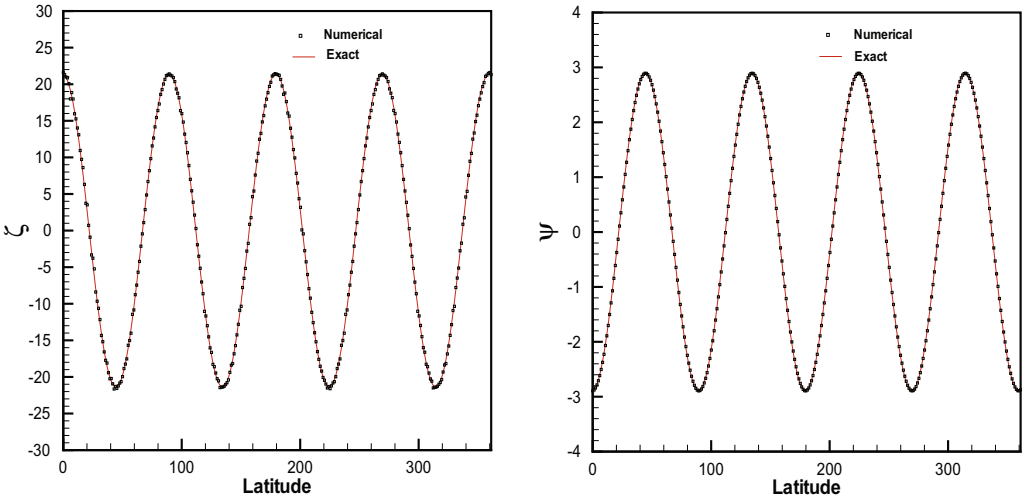

Fig. 5. Comparison of analytical and numerical solutions for the Rossby–Haurwitz wave with cubic interpolation of ζ for the case $L_d = 100$ km at $t = 2\pi/\omega$. Horizontal axes represent latitude is degrees. Right: Stream-function in 10^5 m^2/s. Left: Relative vorticity (in 10^{-8} s^{-1}).

5. VIC in the presence of mean flows

We now describe how to represent the evolution of point vortices in the presence of a background mean flow and associated modifications to the large-scale potential vorticity gradients. For simplicity, here the mean flow is assumed to be zonal and only vary in the meridional direction:

$$\overline{\mathbf{u}} = (\bar{u}(y), 0) \tag{31}$$

The zonal flow is associated with a mean potential vorticity gradient

$$\frac{\partial \overline{Q}}{\partial y} = \beta - \frac{\partial^2 \bar{u}}{\partial y^2} + \frac{\bar{u}}{L_d^2} \tag{32}$$

The evolution of the potential vorticity following the particles is then governed by the equation (written out here in the absence of forcing and dissipation):

$$\frac{DQ'}{Dt} = -v' \frac{\partial \overline{Q}}{\partial y} \tag{33}$$

where Q' is the pv of the particle measured relative to the background and

$$\frac{D}{Dt} = \frac{\partial}{\partial t} + (\overline{\mathbf{u}} + \mathbf{u}') \cdot \nabla$$

is the rate of change following the particle, taking into account the presence of the mean flow. Note that now meridional flow across large-scale gradients in Q, rather than just β, leads to rates of change of Q'.

The above is implemented in the context of VIC as follows. The advection of particles is done as before using a fourth order RK method but this time using the velocity $(\overline{\mathbf{u}} + \mathbf{u}')$. The term $-v' \frac{\partial \overline{Q}}{\partial y}$ is treated as a source term and added to the potential vorticity of particles at both steps of the second order RK time marching scheme.

The dispersion relation of Rossby waves propagating on the mean flow is given by

$$\omega = k\left(\bar{u} - \frac{\overline{Q}_y}{k^2 + l^2 + \frac{1}{L_d^2}}\right) \tag{34}$$

Note that on (large) scales much greater than L_d, Eq. (34) reduces to (neglecting curvature effects in $\overline{Q}_y$)

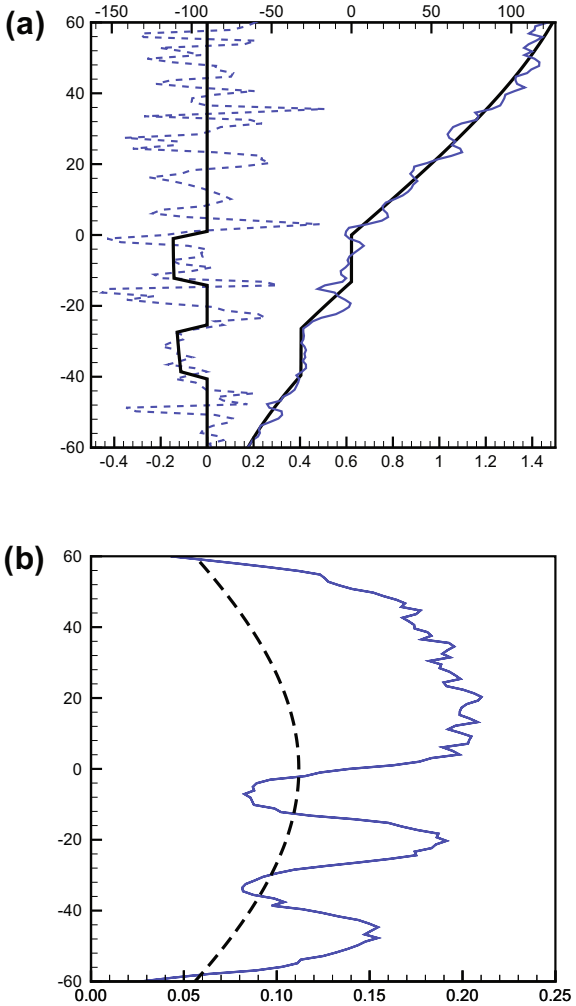

Fig. 6. (a) Meridional sections of the mean flow, $\bar{u}$, (the thick curve) and instantaneous zonal velocity, $\bar{u} + u'$, (thin dashed curve, along a chosen longitude). The scale in m/s is along the lower horizontal axis. Note that $\bar{u}$ is zero everywhere except in two bands where it is equal to $-\beta L_d^2$. The meridional distribution of mean potential vorticity $\overline{Q}$ (thick curve) and instantaneous total potential vorticity, $\overline{Q} + Q'$(thin curve, along the same longitude as chosen to plot the instantaneous u) is also plotted. The scale is on the upper horizontal axis in 10^{-6} s^{-1}. (b) Rossby wave phase speed (dashed thick curve) and u_{rms} (thin curve). The vertical axis is latitude and the horizontal axis is velocity in m/s.

$$\omega = -k\beta L_d^2 \tag{35}$$

i.e., curiously, and as is well known, long Rossby waves are oblivious to mean flow ($\bar{u}$) effects.

In order to study the interaction of mean flow and particles in the context of our VIC model, we set up a mean flow on the sphere which is zero everywhere except in two narrow bands in the southern hemisphere. Inside these bands, the mean flow is set to

$$\bar{u} = -\beta L_d^2 \tag{36}$$

so that the potential vorticity gradients vanish within the bands thus:

$$\overline{Q}_y = \beta + \frac{\bar{u}}{L_d^2} = 0. \tag{37}$$

The $\bar{u}$ and $\overline{Q}$ of the initial state is shown by the thick black lines in Fig. 4.

To represent the growth and decay of baroclinic turbulence on this mean flow we make direct use of the particles and randomly initialize their vorticity thus:

$$\zeta - \psi/L_d^2 = r\zeta^*$$

where $\zeta^* = 10^{-5}\ s^{-1}$, r is a random number between -0.5 and 0.5. The decay of the turbulence thus generated is represented by

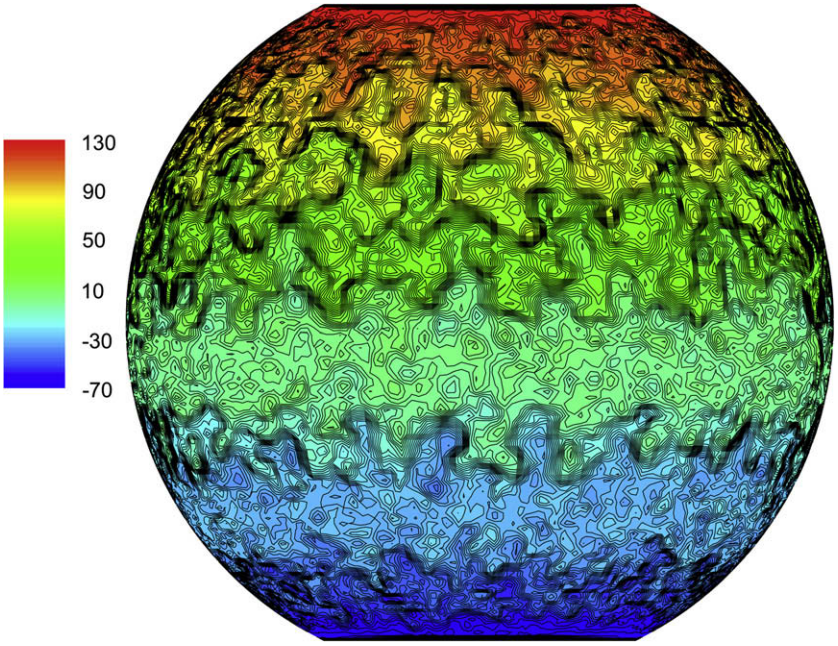

Fig. 7. Instantaneous total potential vorticity, $\overline{Q} + Q'$, in $10^{-6}\ s^{-1}$.

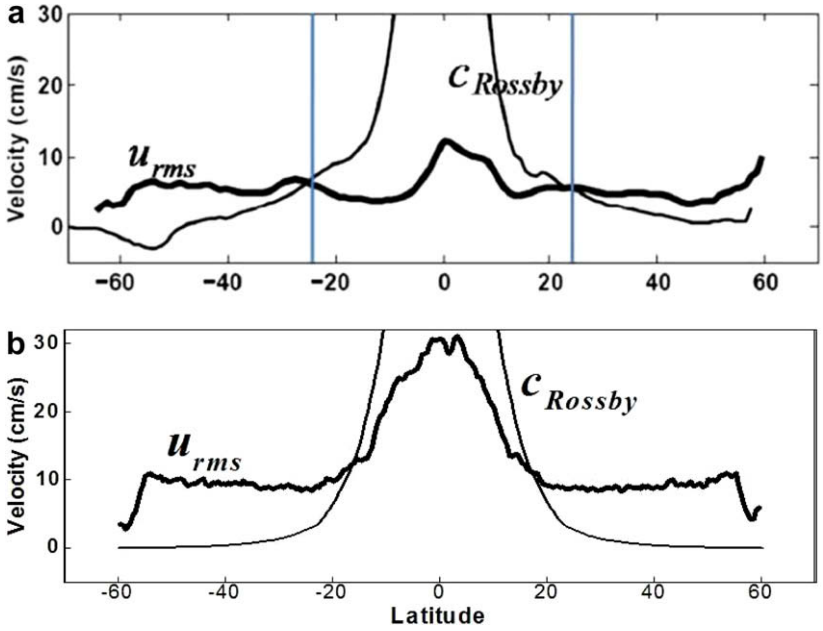

Fig. 8. (a) Rossby wave phase speed, c_{Rossby}, inferred from the propagation of altimetric signals and u_{rms} inferred from surface drifter observations (see Tulloch et al. for more details). (b) c_{Rossby} and u_{rms} from the VIC model.

damping the $\zeta - \psi/L_d^2$ on particles toward zero with an e-folding timescale set to 1 year. When the modulus (normalized by its initial value) becomes smaller than a threshold (chosen to be a factor $1/e$ of the initial value in the corresponding latitude), $\zeta - \psi/L_d^2$ is reset according to the above rule with random signed vorticity. The latitude ranges from -65° to 65° hereafter.

The (gridded) total instantaneous potential vorticity $(\overline{Q} + Q')$ resulting from the deployment of 1.3 million point vortices is shown in Fig. 7 after a period of 20 years in the case $L_d = 80$ km. As is clearly observed, in the southern hemisphere the potential vorticity is well mixed inside the bands and a strong gradient is observed between the two bands. A highly nonlinear regime is also observed in the northern hemisphere. Note that here the circulation spontaneously organises itself in to eastward and westward jets: the eastward flowing jets tend to enhance pv gradients and the westward flowing jets tend to weaken, and indeed often slightly reverse them.

Fig. 6b shows u_{rms}, the rms particle speed relative to the mean flow, as a function of latitude, along with the Rossby wave phase speed, c_{Rossby}, given by Eq. (35). We see that at all latitudes, save for the region of the bands, the nonlinearity parameter $u_{rms}/c_{Rossby} > 1$. This, of course, is consistent with our observation in Fig. 7 that the Q field is strongly distorted by the presence of intense vortices, particularly at high latitudes.

6. Interaction of waves and turbulence on the sphere

In our final illustration of the VIC method, we apply it to the interaction of waves and turbulence in the ocean, a problem which can nicely exploit the dual (vortex, grid) aspects of the numerical approach. The ability to impose rules on the time rate of change of vorticity on discrete particles is again used to simulate the growth (by baroclinic instability) of geostrophic turbulence on the smallest scales resolvable in the model and their subsequent decay. Particle trajectories are readily plotted, as are the stream function and vorticity of their associated flow field on the Eulerian grid.

Recently Tulloch et al. (2009) have argued that the nature of the interaction between geostrophic turbulence and Rossby waves in the ocean depends on whether there is a matching between turbulent and Rossby wave timescales. The interaction between turbulence and waves was explored in the barotropic context by Rhines (1975) (the so-called Rhines effect) and Vallis and Maltrud (1993), and in a (first-mode) baroclinic context applied to the gas planets by Theiss (2004, 2006) and Smith (2004). The central idea is that, as eddies grow in scale in the inverse cascade, their timescale slows, and when this timescale matches the frequency of Rossby waves with the same spatial scale, turbulent energy may be converted into waves. Tulloch et al. (2009) argue that just such a phenomenon controls the interplay of turbulence and waves in the ocean. As shown by the observations plotted in Fig. 8a, at low latitudes the phase speed of first baroclinic mode Rossby waves (c_{Rossby}) far exceeds turbulent velocity scales (u_{rms}), whereas the reverse is true at high latitudes. Thus, one might expect turbulence to generate waves at low latitudes, but not at high latitudes where there is no matching of time scales.

To represent the marked increase in long Rossby wave phase speed as the equator is approached, we specify a meridional variation in L_d in Eq. (1) (small at high latitudes becoming large at low latitudes) to yield a plausible variation in βL_d^2. Note that in contrast to Fig. 5, c_{Rossby} becomes very large (capped at 50 cm/s) as the equator is approached.

As before, to represent the growth and decay of baroclinic turbulence, the vorticity on particles are randomly initialized but according to a slightly different recipe. Since L_d is small at high latitudes, the term $\zeta - \psi/L_d^2$ is dominated by ψ/L_d^2. Hence if a spatially uniform random amplitude for $\zeta - \psi/L_d^2$ is specified,

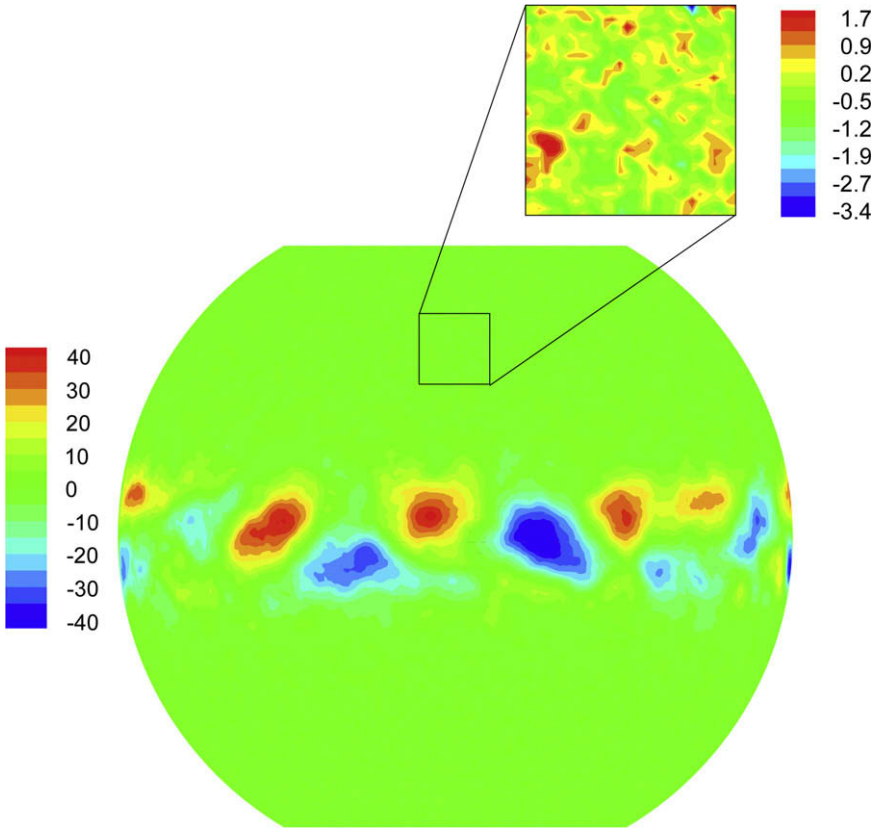

Fig. 9. Stream function plotted in units of 10^4 m^2/s. To reveal the nature of the flow outside the tropical belt, an insert is drawn using a different contour interval.

ψ becomes increasingly small at high latitudes (as L_d decreases) leading to a low level of eddy kinetic energy at high latitudes. This is contrary to observations. Instead we randomly initialize $\zeta - \psi/L_d^2$ thus:

$$\zeta - \psi/L_d^2 = ra\zeta^*$$

where $\zeta^* = 10^{-5}$ s^{-1}, r is a random number between -0.5 and 0.5, and $a = L_d^*/L_d$ is a tuning factor which is larger than unity if L_d is less than L_d^*, a reference deformation radius. This enables us to control the meridional distribution of eddy kinetic energy, bringing it in to broad accord with the observations. A reference L_d^* set equal to 150 km was found to work well.

Figs. 8b and 9 show results in which, as before, 1.3 million particles were employed on the sphere. For the parameters described above, at latitudes outside a tropical band of $\pm 20^\circ$, u_{rms} drops below c_{Rossby}. In the tropical band the turbulence generates waves: the flow becomes organized in to large-scale Rossby waves that propagate westward at the long Rossby wave phase speed. Outside the tropical band, by contrast, no such organization is observed and the flow is dominated by the turbulent wandering of vortices—see insert in Fig. 9. This is very clear on inspection of the trajectory of individual particles in the tropical and high latitude bands shown in Fig. 10.

7. Conclusions

A vortex in cell model for quasi-geostrophic, shallow water dynamics on the sphere has been presented. It was shown that special attention must be paid to the interpolation of data from particles to the Eulerian grid and vice versa, particularly for modeling of slow oceanic dynamics. Numerical experiments were performed to evaluate the performance of the model in simulation of Rossby waves on the sphere and encouraging results were obtained for both oceanic and atmospheric problems. Stability, accurate Lagrangian modeling of the advection of vorticity and conservation of potential vorticity, leads to an accurate and efficient tool for the study of the interaction of waves, vortices and mean flows in the presence of boundaries.

To illustrate the potential applications of this new tool which exploit the particle/grid duality of the numerical method, we described two experiments in which baroclinic instability was represented by introducing a vorticity charge–discharge cycle to parameterize the growth and decay of pv anomalies associated with the instability. In the first application we prescribed mean flows and mean pv gradients and observed the evolution of vortices on this background flow. In the second application we studied the interaction of waves and turbulence on the sphere in the case where, as is observed, the deformation radius becomes large and hence first baroclinic Rossby waves propagate very fast, as

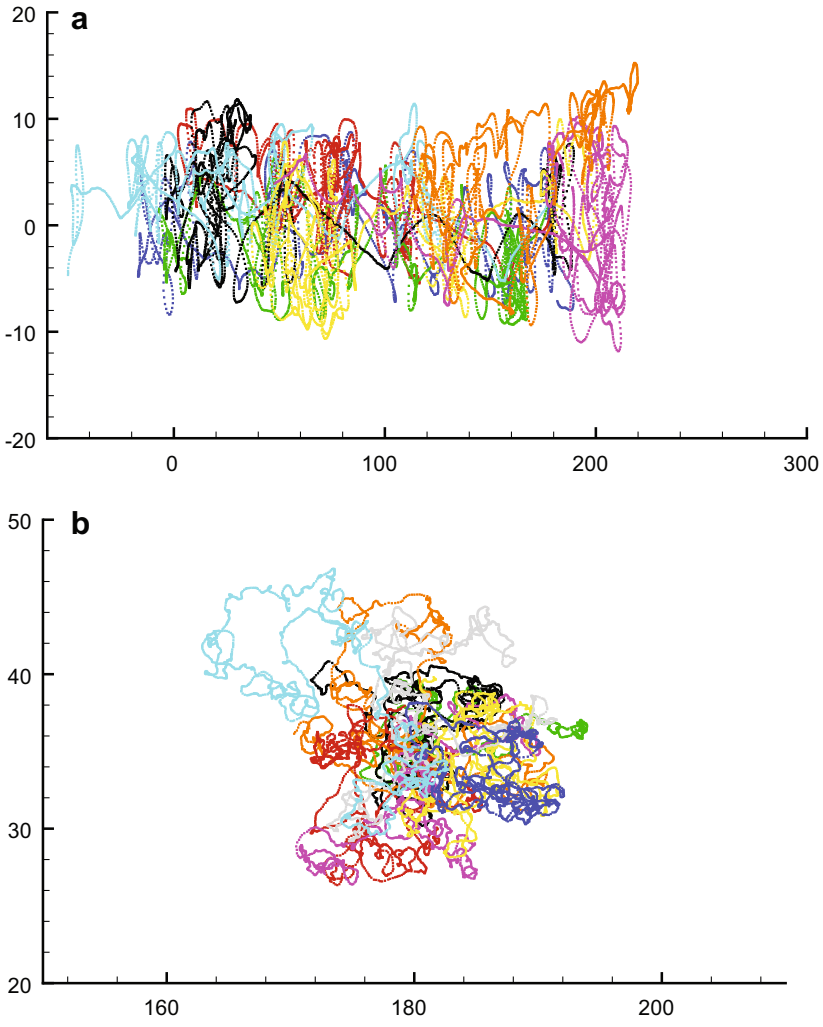

Fig. 10. Particle trajectories (a) in the equatorial band and (b) in high latitudes. Horizontal and vertical axes represent longitude and latitude, respectively.

the equator is approached. We found that turbulence generates waves in the tropical band where $c_{Rossby} > u_{rms}$, but not at higher latitudes where the reverse is true.

Finally, it should be said that extension to more than one layer and introduction of geometrical constraints (coasts and islands) in the context of VIC is no more complicated than in standard quasi-geostrophic models.

Acknowledgements

We thank the Physical Oceanography program of the US National Science Foundation for support of this study. It is part of our contribution to the DIMES experiment.

Appendix A. The area and cubic Lagrange interpolation methods

In the area method, a vorticity of magnitude unity is credited to the four surrounding grid points by (see, e.g. Christiansen, 1973; Liu and Doorly, 1999)

$$\zeta(i,j) = A_1, \qquad \zeta(i+1,j) = A_2 \tag{38}$$

$$\zeta(i,j+1) = A_3, \qquad \zeta(i+1,j+1) = A_4 \tag{39}$$

and is superimposed for all particles. The coefficients A_1 to A_4 are given in (13), (14). A weighting factor should be also applied based on the initial number of particles in each cell.

In the cubic Lagrange interpolation method, given $f(x_1), f(x_2), f(x_3)$ and $f(x4)$, the function $f(x)$ is approximated as

$$f(x) = c_1 f(x_1) + c_2 f(x_2) + c_3 f(x_3) + c_4 f(x_4) \tag{40}$$

where

$$c_1 = \frac{(x-x_2)(x-x_3)(x-x_4)}{(x_1-x_2)(x_1-x_3)(x_1-x_4)} \tag{41}$$

$$c_2 = \frac{(x-x_1)(x-x_3)(x-x_4)}{(x_2-x_1)(x_2-x_3)(x_2-x_4)} \tag{42}$$

$$c_3 = \frac{(x-x_1)(x-x_2)(x-x_4)}{(x_3-x_1)(x_3-x_2)(x_3-x_4)} \tag{43}$$

$$c_4 = \frac{(x-x_1)(x-x_2)(x-x_3)}{(x_4-x_1)(x_4-x_2)(x_4-x_3)} \tag{44}$$

References

Christiansen, J.P., 1973. Numerical simulation of hydrodynamics by the method of point vortices. Journal of Computational Physics 13, 363–379.

Cocle, R., Winckelmans, G., Daeninck, G., 2008. Combining the vortex-in-cell and parallel fast multipole methods for efficient domain decomposition simulations. Journal of Computational Physics 227, 9091–9120.

Cottet, G.-H., Koumoutsakos, P., 2000. Vortex Methods: Theory and Practice. Cambridge University Press, Cambridge, UK.

Cottet, G.-H., Michaux, B., Ossia, S., VanderLinden, G., 2002. A comparison of spectral and vortex methods in three-dimensional incompressible flows. Journal of Computational Physics 175, 702–712.

Cottet, G.-H., Poncet, P., 2003. Advances in direct numerical simulations of 3D wall-bounded flows by Vortex-in-Cell methods. Journal of Computational Physics 193, 136–158.

Huang, M.-J., Chen, L.-C., Su, H.-X., 2009. A fast resurrected core-spreading vortex method with no-slip boundary conditions. Journal of Computational Physics 228 (6), 1916–1931.

Kudela, H., Regucki, P., 2002. The vortex-in-cell method for the study of three-dimensional vortex structures. In: Bajer, K., Moffatt, H.K. (Eds.), Tubes, Sheets and Singularities in Fluid Dynamics. Kluwer Academic Publishers, The Netherlands, pp. 49–54.

Lakkis, I., Ghoniem, A., 2009. A high resolution spatially adaptive vortex method for separating flows. Part I: Two-dimensional domains. Journal of Computational Physics 228 (2), 491–515.

Liu, C.H., Doorly, D.J., 1999. Velocity–vorticity formulation with vortex particle-in-cell method for incompressible viscous flow simulation. Part I: Formulation and validation. Numerical Heat Transfer Part B 35, 251–275.

Liu, C.H., 2001. A three-dimensional vortex particle-in-cell method for vortex motions in the vicinity of a wall. International Journal for Numerical Methods in Fluids 37, 501–523.

Ould-Salihi, M.L., Cottet, G.-H., El Hamraoui, M., 2000. Blending finite-difference and vortex methods for incompressible flow computations. SIAM Journal of Scientific Computing 22 (5), 1655–1674.

Rhines, P.B., 1975. Waves and turbulence on a β-plane. Journal of Fluid Mechanics 69, 417–443.

Smith, K.S., 2004. A local model for planetary atmospheres forced by small-scale convection. Journal of Atmospheric Sciences 61, 1420–1433.

Theiss, J., 2004. Equatorward energy cascade, critical latitude, and the predominance of cyclonic vortices in geostrophic turbulence. Journal of Physical Oceanography 34, 1663–1678.

Theiss, J., 2006. A generalized Rhines effect on storms on Jupiter. Geophysical Research Letters 33, L08. 809.

Tulloch, R., Marshall, J., Smith, K.S., 2009. Interpretation of the propagation of surface altimetric observations in terms of planetary waves and geostrophic turbulence. Journal of Geophysical Research 114, C02005. doi:10.1029/2008JC005055.

Uchiyama, T., Naruse, M., 2004. Numerical simulation for gas-particle two-phase free turbulent flow based on vortex in cell method. Powder Technology 142, 193–208.

Vallis, G.K., Maltrud, M.E., 1993. Generation of mean flows and jets on a beta plane and over topography. Journal of Physical Oceanography 23, 1346–1362.

Williamson, D.L., Drake, J.B., Hack, H.J., Jakob, R., Swarztrauber, P.N., 1992. A standard test set for numerical approximations to the shallow water equations in spherical geometry. Journal of Computational Physics 102, 211–224.